Nudged elastic band approach to nuclear fission pathways

Eric Flynn[1], Daniel Lay[1], Sylvester Agbemava[2], Pablo Giuliani[2,3], Kyle Godbey[2]
Witold Nazarewicz[1], and Jhilam Sadhukhan[4,5]

[1]*Department of Physics and Astronomy and FRIB/NSCL Laboratory, Michigan State University, East Lansing, Michigan 48824, USA*
[2]*FRIB/NSCL Laboratory, Michigan State University, East Lansing, Michigan 48824, USA*
[3]*Department of Statistics and Probability, Michigan State University, East Lansing, Michigan 48824, USA*
[4]*Physics Group, Variable Energy Cyclotron Centre, Kolkata 700064, India*
[5]*Homi Bhabha National Institute, Mumbai 400094, India*

Background: The nuclear fission process is a dramatic example of the large-amplitude collective motion in which the nucleus undergoes a series of shape changes before splitting into distinct fragments. This motion can be represented by a pathway in the many-dimensional space of collective coordinates. Within a stationary framework rooted in a static collective Schrödinger equation, the collective action along the fission pathway determines the spontaneous fission half-lives as well as mass and charge distributions of fission fragments.

Purpose: We study the performance and precision of various methods to determine the minimum-action and minimum-energy fission trajectories in the collective space.

Methods: We apply the nudged elastic band method (NEB), grid-based methods, and the Euler-Lagrange approach to the collective action minimization in two- and three-dimensional collective spaces.

Results: The performance of various approaches to the fission pathway problem is assessed by studying the collective motion along both analytic energy surfaces and realistic potential-energy surfaces obtained with the Skyrme-Hartree-Fock-Bogoliubov theory. The uniqueness and stability of the solutions is studied. The NEB method is capable of efficient determination of the exit points on the outer turning surface that characterize the most probable fission pathway and constitute the key input for fission studies. This method can also be used to accurately compute the critical points (i.e., local minima and saddle points) on the potential-energy surface of the fissioning nucleus that determine the static fission path. The dynamic programming method also performs quite well and it can be used in many-dimensional cases to provide initial conditions for the NEB calculations.

Conclusions: The NEB method is the tool of choice for finding the least-action and minimum-energy fission trajectories. It will be particularly useful in large-scale static fission calculations of superheavy nuclei and neutron-rich fissioning nuclei contributing to the astrophysical *r*-process recycling.

I. INTRODUCTION

Fission is a fundamental nuclear decay that is important in many areas of science, ranging from structure and stability of heavy and superheavy nuclei [1–3] to studies devoted to physics beyond the standard model of particle physics [4] and the synthesis of heavy elements [5–7].

Theoretically, the nuclear fission process is an example of the nuclear large-amplitude collective motion originating from the single-particle motion of individual nucleons. Due to the complexity of this process, our understanding of nuclear fission is still incomplete. For the state of affairs in this field, we refer to the recent review [8,9].

When it comes to realistic predictions, the self-consistent nuclear energy density-functional (EDF) method [10,11] has proven to be very successful in terms of quantitative reproduction of fission lifetimes and fragment yields. Unfortunately, realistic self-consistent fission calculations in multidimensional collective spaces, based on the microscopic input,

are computationally expensive when it comes to large-scale theoretical fission surveys. Given the computational cost of microscopic methods and the large number of fissioning nuclei that are, e.g., expected to contribute to the astrophysical *r*-process nucleosynthesis, calculations have mostly relied on simple parametrizations or highly phenomenological models. The new perspective is offered by state-of-the-art theoretical frameworks and modern computational techniques that promise to speed up the calculations to be able to carry out quantified global fission surveys for multiple inputs [9].

This study is concerned with finding the optimal pathway during the tunneling motion phase of spontaneous fission (SF). Within a static collective Schrödinger equation framework, such a trajectory, dubbed the least-action path (LAP), is obtained by minimizing the collective action in a many-dimensional collective space [12,13]. A number of techniques have been proposed to deal with this challenging task. In the early application [14], the trial pathways were assumed in a parametrized form and the LAP was obtained by minimizing

the penetration integral with respect to the variational parameters. Grid-based techniques such as the dynamic programming [15] and Ritz [16] methods have been used in numerous EDF calculations of LAPs [17–23]. In Refs. [24–29], LAPs were obtained by solving the eikonal equation by the method of characteristics. Effectively, this method can be related to the instanton approach: a quantum-mechanical propagation in imaginary time that amounts to solving the classical equations of motion in an inverted potential. Only one solution of the eikonal equations, called the escape path, arrives at the *exit point* on the outer turning surface with zero velocity. Other trajectories, corresponding to different initial conditions, cannot reach the outer turning surface. For the recent applications of the instanton framework to fission, we refer the reader of Refs. [30–32]. Up to now, however, applications of this method to nuclear physics problems have been limited because of enormous numerical difficulties [30,33].

In this paper, we compare grid-based approaches to the LAPs with the nudged elastic band (NEB) method that was originally formulated in the context of molecular systems [34–37]. In NEB, the minimum action path can be obtained iteratively by continuously shifting the pathway to the nearest minimum action path [38–40]. A similar approach is a growing string method [41]. To provide more insights, we also employ the Euler-Lagrange (EL) method to compute the stationary action path.

In addition to the LAP, another characteristic trajectory in the collective space is the minimum-energy path (MEP), sometimes referred to as the static path. The MEP can serve as a first, rough approximation to the LAP. It is obtained by computing the steepest descent line on the potential-energy surface, which passes through the local minima and saddle points. To find the MEP, a flooding, or watershed, algorithm has been applied [42–46]. The NEB approach can also be adopted to find the MEP and saddle points [47]. (For a review of modern optimization methods for finding MEPs, see Refs. [48,49].)

This paper is organized as follows: In Sec. II we define the basics concepts of the nuclear EDF approach as applied to nuclear fission. Section III describes the path-optimization methods used. The results of our calculations and an analysis of trends are presented in Sec. IV. Finally, Sec. V contains the conclusions of this work.

II. NUCLEAR ENERGY DENSITY FUNCTIONAL APPROACH TO SPONTANEOUS FISSION

The main ingredients for a theoretical determination of SF lifetimes are the collective potential-energy surface (PES) and the inertia tensor. To compute the PES, one solves the constrained Hartree-Fock-Bogoliubov (HFB) equations with the realistic energy density functional in the space of collective coordinates $\boldsymbol{q} \equiv \{q_i\}$. These are usually represented by the expectation values of the quadrupole moment operator $\hat{Q}_{20}$ (elongation), quadrupole moment operator $\hat{Q}_{22}$ (triaxiality), octupole moment operator $\hat{Q}_{30}$ (mass asymmetry), and the particle-number dispersion term $\lambda_{2\tau}(\hat{N}_\tau^2 - \langle \hat{N}_\tau \rangle^2)$ ($\tau = n, p$) that controls dynamic pairing correlations [18,50,51]. In some cases one also considers the hexadecapole moment Q_{40}

(necking coordinate) [52]. That is, in practical applications, we consider 2–5 collective coordinates which describe the collective motion of the system. Figure 1 shows a representative PES of ^{256}Fm in the space of $Q_{20} \equiv \langle \hat{Q}_{20} \rangle$ and $Q_{30} \equiv \langle \hat{Q}_{30} \rangle$.

The collective inertia (or mass) tensor $\mathcal{M}_{ij}(\boldsymbol{q})$ is obtained from the self-consistent densities by employing the adiabatic time-dependent HFB approximation (ATDHFB) [56–58]. In this study, we use the nonperturbative cranking approximation [56]:

$$\mathcal{M}_{ij}(\boldsymbol{q}) = \frac{\hbar^2}{2\dot{q}_i\dot{q}_j} \sum_{\alpha\beta} \frac{\left(F_{\alpha\beta}^{i*}F_{\alpha\beta}^{j} + F_{\alpha\beta}^{i}F_{\alpha\beta}^{j*}\right)}{E_\alpha + E_\beta}, \quad (1)$$

where q_i is the collective coordinate, $\dot{q}_i$ represents the time derivative of q_i, and E_α are one-quasiparticle energies of HFB eigenstates $|\alpha\rangle$. The matrices F^i are given by

$$\frac{F^{i*}}{\dot{q}_i} = A^T \frac{\partial \kappa^*}{\partial q_i} A + A^T \frac{\partial \rho^*}{\partial q_i} B - B^T \frac{\partial \rho}{\partial q_i} A - B^T \frac{\partial \kappa}{\partial q_i} B, \quad (2)$$

where A and B are the matrices of the Bogoliubov transformation, and ρ and κ are particle and pairing density matrices, respectively, determined in terms of A and B. Derivatives of the density matrices with respect to collective coordinates are calculated by employing the three-point Lagrange formula. It is important to remark that rapid variations in $\mathcal{M}_{ij}$ are expected in the regions of configuration changes (level crossings) due to strong variations of density derivatives in (2) associated with structural rearrangements [14,17].

Since SF is a quantum-mechanical tunneling process and the fission barriers are usually both high and wide, the SF lifetime is obtained semiclassically [13] as $T_{1/2} = \ln 2/(nP)$, where n is the number of assaults on the fission barrier per unit time and P is the penetration probability given by

$$P = (1 + \exp[2S(L_{\min})])^{-1}, \quad (3)$$

where $L_{\min}$ is the path that minimizes the fission action integral calculated along the one-dimensional trajectory $L(s)$ in the multidimensional collective space:

$$S(L) = \frac{1}{\hbar} \int_{s_{in}}^{s_{out}} \mathcal{S}(s) ds, \quad (4)$$

where

$$\mathcal{S}(s) = \sqrt{2\mathcal{M}_{eff}(s)[V_{eff}(s) - E_0]} \quad (5)$$

with $V_{eff}(s)$ and $\mathcal{M}_{eff}(s)$ being the effective potential energy and inertia along the fission path $L(s)$, respectively. V_{eff} can be obtained by subtracting the vibrational zero-point energy from the total HFB energy. (In the examples considered in this paper we assume the zero-point energy to be zero.) The integration limits s_{in} and s_{out} correspond to the classical inner and exit points, respectively, defined by $V_{eff}(s) = E_0$ on the two extremes of the fission path, see Fig. 1. The collective ground state (g.s.) energy is E_0, and ds is the element of length along $L(s)$. A one-dimensional path $L(s)$ can be defined in the multidimensional collective space by specifying the collective variables $\boldsymbol{q}(s)$ as functions of path's length s. The expression
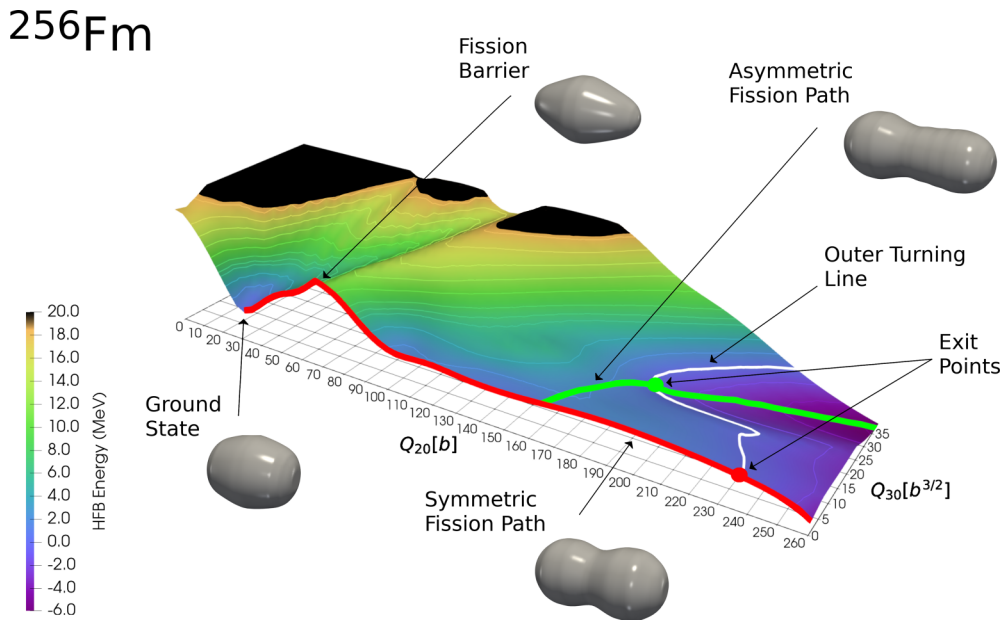
FIG. 1. Potential-energy surface of ^{256}Fm calculated with nuclear EDF method using the D1S parametrization of the Gogny interaction [53] in the space of two collective coordinates: Q_{20} (elongation) and Q_{30} (mass asymmetry). The static fission pathways are marked by solid lines: red (symmetric pathway) and green (asymmetric pathway). The outer turning line (OTL) is indicated, together with the exit points associated with the static pathways. For simplicity, we assume that the inner turning point corresponds to the ground-state configuration (i.e., $E_0 = 0$). The high-energy region that is practically not accessible during collective motion is indicated in black. The intersections of fission pathways with exit points are indicated by dots; these are important for determining fission-fragment yields [54,55].

for $\mathcal{M}_{\text{eff}}$ is [59]:

$$\mathcal{M}_{\text{eff}}(s) = \sum_{ij} \mathcal{M}_{ij}(\boldsymbol{q}) \frac{dq_i}{ds} \frac{dq_j}{ds}. \quad (6)$$

The least-action path (LAP) L_{min} is obtained by minimizing the action integral (4) with respect to all possible trajectories L that connect the lines and surfaces of inner turning points s_{in} and exit points s_{out} [17]. However, as discussed in Refs. [24,25] and this paper, only the pathways related to the exit points are stationary. The MEP can instead be described as the union of steepest descent paths from the saddle point(s) to the minima. The corresponding trajectory $\boldsymbol{q}(s)$ satisfies

$$\frac{d\boldsymbol{q}}{ds} \propto \nabla V(\boldsymbol{q}(s)), \quad (7)$$

which characterizes a path of steepest descent on a surface $V(\boldsymbol{q})$ [60]. For the NEB, one finds the MEP by allowing the elements of the path to follow the gradient of the PES in their immediate vicinity. We shall assume that the PES in the tunneling region is free from discontinuities associated with rapid configuration changes [61–63]. This assumption is usually valid because of nonvanishing pairing correlations inside the potential barrier. It is also to be noted that, as in any optimization or minimization approach, the stationary path determined numerically corresponds to a local action minimum, which is not guaranteed to be the global minimum. Moreover, there could be many stationary pathways representing different fission modes, see Fig. 2. To simplify notation, we assume in the following discussions that the stationary action path found by our algorithms is indeed the LAP.

Since $\mathcal{S}(s) = 0$ on the outer turning surface $V(\boldsymbol{q}) = E_0$, it follows that paths moving on the surface $V(\boldsymbol{q}) = 0$ do not
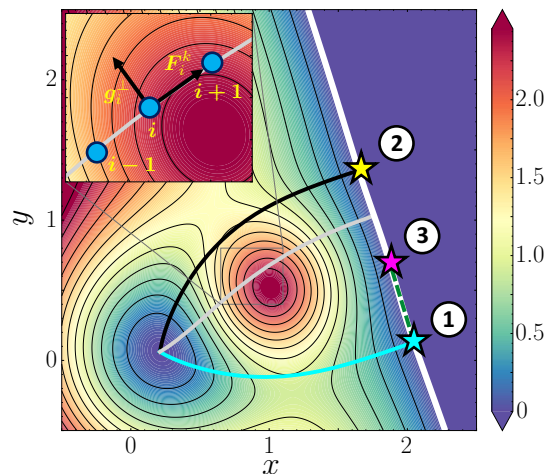

FIG. 2. Illustration of two stationary action paths (representing competing fission modes) from the g.s. to the OTL (marked white) on the PES given by Eq. (12). The cyan line shows the primary path (1). The secondary path (2) is indicated by the black line. The corresponding exit points are marked by stars. The green dashed line connects the exit point (1) with the point (3) on the OTL; the action along the dashed path is zero. The inset shows the spring force and the action force acting on the image i on the NEB for the intermediate (not fully converged) gray path. For the video illustrating the NEB determination of both LAPs, see the Supplemental Material (SM) [64].

contribute to the action. This is illustrated in Fig. 2 by the path connecting the g.s. and, for example, the purple star labeled (3). Such a path consists of the cyan curve—the exit trajectory—and the green dashed line, connecting (1) with (3) through the OTL, which results in the same action integral as the exit trajectory.

III. METHODS AND ALGORITHMS

All path-optimization methods described in the following sections, but the EL method, have a reference implementation included in the python package, PyNEB [65], which has been developed by the authors for this work.

A. Nudged elastic band

The NEB method was originally formulated to provide a smooth transition of a molecular system on a potential-energy surface from the reactant to the product state [35–37]. Upon application of this variant of the NEB method, one obtains the MEP as well as a series of "images" of the molecular system as it transitions along the path. The NEB technique has been subsequently refined, with improved numerical stability [39] and a more accurate determination of a saddle point [38] being two key advances towards a more widely applicable numerical approach for MEP determination.

To obtain the LAP, the procedure must be modified such that the images move towards the minimum of the action [66] which amounts to replacing the standard gradient of the PES with the gradient of the action

$$g_i = -\nabla_i S, \tag{8}$$

with respect to the image q_i. With this prescription, the images will settle to the LAP in the collective space.

While the NEB method will, by design, drive the line of images towards either the MEP or LAP, the iterative scheme chosen greatly impacts the total number of iterations required before the solution converges. In the early implementations, a simple velocity Verlet algorithm [67] was used to adjust the position of the images step to step [35–39]. This approach is robust and relatively stable, although the convergence can be slow for flatter surfaces where the images are not pulled strongly to their optimal positions. To aid this process, the fast inertial relaxation engine (FIRE) was proposed [68] to accelerate convergence without sacrificing stability. The method was subsequently updated [69] to further improve performance. Indeed, in our tests, the inertial algorithm regularly outperforms the velocity Verlet algorithm by an-order-of-magnitude reduction in iterations at the same convergence criteria.

With this, our implementation of the NEB approach is defined. The algorithm itself is outlined in Algorithm 1 in the SM [64]. The force used in the optimization step for each image, F_i^{opt}, is constructed by adding the perpendicular component of the action gradient to the spring force F_i^k between the images,

$$F_i^k = k(|q_{i+1} - q_i| - |q_i - q_{i-1}|)\tau_i, \tag{9}$$

where k is a tunable parameter that controls the strength of the spring force and τ_i is the unit vector tangent to the line of images from image $i - 1$ to image $i + 1$. The spring force on the endpoints is defined differently:

$$F_1^k = k|q_2 - q_1|, \quad F_N^k = k|q_N - q_{N-1}|. \tag{10}$$

The total force acting on the interior images is then

$$F_i^{\text{opt}} = F_i^k + g_i^\perp. \tag{11}$$

The NEB approach is illustrated in Fig. 2 for the case of bimodal tunneling from the g.s. minimum to the OTL on an analytic PES defined by

$$V(q) = 3.17 + 2e^{-5[(x-1)^2 + (y-\frac{1}{2})^2]} - 3e^{-(x^2+y^2)}$$
$$- \frac{1}{2}(3x + y), \tag{12}$$

where $q = (x, y)$. The inset shows the forces on the images of the NEB gray path, which has not converged yet to the black path. The spring force F_i^k keeps the images from drifting too much from each other, while the perpendicular part of the action gradient $g_i^\perp$ pushes them towards the nearest stationary action path. This example shows that the NEB algorithm, depending on the initial locations of the images, will converge to a local stationary path, not necessarily the least action path.

For the endpoint, $i = N$, one can choose to either fix the position of the image or to allow the image to move towards the outer turning surface. In the second case, a harmonic restraint term is added to the spring force to construct F_N^{opt},

$$F_N^{\text{opt}} = F_N^k - \{F_N^k \cdot f(q_N) - \eta[V(q) - E]\}f(q_N), \tag{13}$$

where $f = -\nabla V / |\nabla V|$ and η determines the strength of the harmonic restraint term [66]. This force pulls the endpoint $i = N$ very quickly to the outer turning surface and helps find the optimal exit points.

The default iteration scheme used in our implementation is the inertial algorithm mentioned above, although a standard Verlet minimizer is also included in the PyNEB python package [65]. The structure of the NEB solver is modular and allows for the simple replacement of components like the minimizer, allowing for easy checks on the convergence and parameters that describe the iterative scheme.

B. Grid-based methods

Some traditional methods to compute the LAP begin by computing the PES and the collective inertia on a grid of collective coordinates. The calculation of the LAP is then reduced to finding the path through the grid points that minimizes a discrete approximation of the action. Two methods that we have benchmarked are the dynamic programming method (DPM) [15], and Dijkstra's algorithm (DA) [70]. Here, both will be described for two-dimensional (2D) grid, with points labeled by $q_{ij} = (x_i, y_j)$ ($i = 1, \ldots, N$, $j = 1, \ldots, M$). Both methods can be straightforwardly extended to a higher-dimensional grid.

Dynamic programming is a general mathematical technique for solving multidecision problems by breaking the
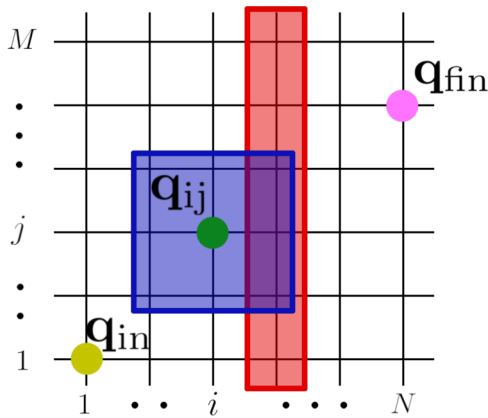
FIG. 3. Different types of paths that can be found in the different grid-based methods. The single node q_{ij} can reach the red (blue) regions in DPM (DA). The initial and final points are marked.

problem down into simpler overlapping subproblems. It was first adapted to the action integral minimization in Ref. [15] and used in Ref. [17] to determine the LAP. This adaptation is what we refer to as the DPM.

The DPM approximates the LAP between an initial point q_{in} and a final point q_{fin}. This method finds paths that traverse diagonally from a given cell: from cell q_{ij}, only cells $q_{i+1,j}$ can be reached, for $j = 1, \ldots, M$. The allowed cells are highlighted in red in Fig. 3. The LAP from q_{in} to q_{fin} is constructed iteratively as follows: for a cell q_{ij}, there are M possible paths, each passing through a cell at x_{i-1}. The LAP from q_{in} to q_{ij} is selected and stored in memory. This is repeated for every cell with $x = x_i$, for a total of M possible paths. Once q_{fin} is reached, there are only MN paths (out of a total of M^N paths), and the LAP is selected from these. The DPM algorithm is detailed in Algorithm 2 in the SM [64].

Dijkstra's method [70] is similar to DPM, in that it breaks down the large optimization problem into a set of smaller problems. Given a cell q_{ij}, the action to every neighbor $q_{i'j'}$ is calculated as if the path to $q_{i'j'}$ passes through q_{ij}. If this action integral is smaller than that along the current path to $q_{i'j'}$, $q_{i'j'}$ is said to come from q_{ij}. This is repeated, starting from q_{in}, until q_{fin} is reached. Figure 3 shows the nearest-neighbors of q_{ij} (the cell marked in green) in a blue square. Dijkstra's algorithm is described in Algorithm 3 in the SM [64].

Dijkstra's algorithm can find paths that pass through multiple cells with the same x_i value, or even paths that backtrack. DPM cannot find such paths. However, DPM can find paths that jump from q_{ij} to $q_{i+1,j'}$, for any j', while Dijkstra's algorithm is limited to $j' = j - 1, j, j + 1$ (see Fig. 3). For fission calculations, one frequently takes the x coordinate as the quadrupole moment Q_{20}, and fission can be viewed as collective motion in which Q_{20} continuously increases towards scission. So, the paths that Dijkstra's algorithm can find, that DPM cannot, are rather unlikely. In general DPM tends to find paths with a smaller action than Dijkstra's algorithm, see Sec. IV.

C. Euler-Lagrange equations

To find the LAP for the functional (4) using the EL equations [71], we first parametrize the trajectory q by a time variable t, i.e., $q = q(t)$ with $t \in [0, t_f]$. This is done in order to explicitly account for the arclength $ds = (\sum dq_i^2)^{1/2}$. In terms of t, the action integral (4) reads:

$$S(L) = \int_0^{t_f} \sqrt{2(V_{\text{eff}}[q(t)] - E_0)} \left(\sum_{ij}^n \mathcal{M}_{ij}[q(t)]\dot{q}_i\dot{q}_j \right)^{1/2} dt$$

$$= \int_0^{t_f} \mathcal{L}(q, \dot{q})dt, \tag{14}$$

where $\dot{q}_i \equiv dq_i/dt$, and $\mathcal{L}$ is the corresponding Lagrangian. The associated EL equation can be written as

$$\frac{\partial \mathcal{L}}{\partial q_i} = \frac{d}{dt}\left(\frac{\partial \mathcal{L}}{\partial \dot{q}_i}\right), \tag{15}$$

with the boundary conditions: $q(t = 0) = q_{in}$ (the initial location) and $q(t = t_f) = q_{fin}$ (the final location).

To numerically solve Eq. (15) we use the shooting method [72]. That is, we start at the initial position q_{in} and vary the direction and orientation of the initial "velocity" $\dot{q}(t = 0)$. We use a numerical differential equation solver to propagate the solution until we find an initial condition that satisfies $q(t_f) = q_{fin}$. Finding such initial conditions can present some challenges, which we discuss in the SM [64].

The EL approach is equivalent to what is done in Ref. [24] where the eikonal equation is solved by the method of characteristics. Each different trajectory obtained by varying $\dot{q}(t = 0)$ corresponds to one of the characteristics of the leading order [cf. Eqs. (2.8) and (4.3) of Ref. [24]]. It is worth noting that if the imaginary part of the phase of the wave function $W(q)$ is negligible, as is the case of the motion in the deep subbarrier region, then the eikonal equation for W is a valid approximation [12]. The trajectories corresponding to the stationary functional (4) are equivalent to the solutions of the eikonal equation for W [see Eqs. (11) and (13) of Ref. [12]]. A connection between the eikonal equation, the dynamic programming approach, and a variational principle in the context of geometrical optics is discussed in Ref. [73].

IV. RESULTS

A. Analytic surfaces: Illustrative examples

We benchmark the performance of the NEB method by comparing the LAP found using NEB (denoted as NEB-LAP) to the paths found using the DPM, DA, and EL approaches for analytic surfaces defined in terms of the position vector $q = (x, y)$. Throughout this section, we assume a constant inertia $\mathcal{M}_{ij} = \delta_{ij}$. Within the NEB framework, the action functional (4) can develop some noise as the NEB algorithm approaches the final action. This noise is a function of the NEB hyperparameters and the optimization method used. All surfaces discussed in this section are released as example cases with PyNEB [65].

In the analytic cases, the NEB is initialized by fixing an initial and final points q_{in} and q_{fin}, respectively, and defining a linear trajectory connecting them. The NEB algorithm is then

TABLE I. Action integrals for the six-camel-back (CB-S and CB-A) and Müller-Brown (MB) surfaces. The integrals have been calculated using a linear spline interpolation evaluated at 500 points along each trajectory.

	NEB-MEP	NEB-LAP	DPM	EL	DA
CB-S	5.522	5.518	5.524	5.536	5.563
CB-A	6.793	6.404	6.405	6.407	6.886
MB	28.491	22.875	22.909	22.871	23.427

iterated until convergence is reached. Grid-based methods use a grid spacing of $\Delta x = 0.1$ along the x axis and $\Delta y = 0.005$ along the y axis for all analytic surfaces. Details of the numerical methods used for solving the EL equations for all surfaces are discussed in the SM [64]. The action values for each surface considered are included in Table I. Action integrals in Table I are evaluated by using linearly interpolated trajectories over 500 uniformly distributed points.

We compute both LAP and MEP in the NEB framework. Since the MEP is a solution of Eq. (7), images along the path converge to critical points on the surface depending on the position of the boundary images at $\boldsymbol{q}_{\rm in}$ and $\boldsymbol{q}_{\rm fin}$. Critical points on the surface $V(\boldsymbol{q})$ contained in the MEP can be extracted by calculating ∇V along the path and are classified by computing the eigenvalues of the Hessian at those points.

First, we consider the symmetric six-camel back potential (CB-S) [49] defined as

$$V_{\rm CB\text{-}S}(\boldsymbol{q}) = \left(4 - 2.1x^2 + \tfrac{1}{3}x^4\right)x^2 + xy + 4(y^2 - 1)y^2. \tag{16}$$

In this example, we seek the LAP connecting the local minimum located at $\boldsymbol{q}_{\rm in} = (1.70, -0.79)$ to the local minimum located at $\boldsymbol{q}_{\rm fin} = (-1.70, 0.79)$. Figure 4 shows the CB-S PES normalized to zero at its global minimum together with the calculated NEB-MEP, NEB-LAP, DPM, EL, and DA trajectories. The action integrals along these trajectories are listed
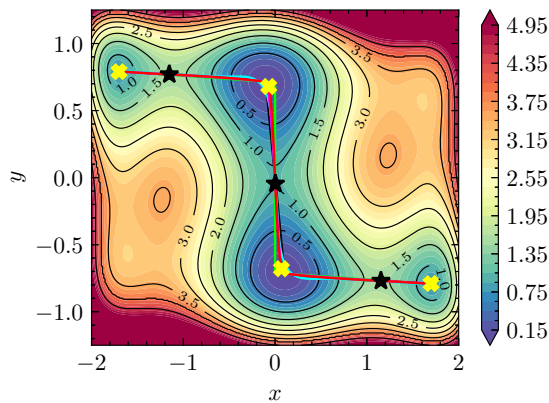

FIG. 4. The symmetric camel-back PES $V_{\rm CB\text{-}S}(\boldsymbol{q})$ normalized to its global minimum together with the calculated NEB-MEP (red), NEB-LAP (magenta), DPM (black), EL (cyan), and DA (lime) trajectories. Black stars indicate saddle points and yellow crosses mark local minima.
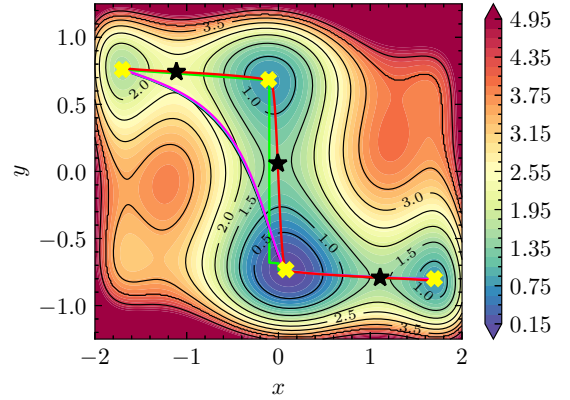

FIG. 5. Similar as in Fig. 4 but for the asymmetric camel-back surface $V_{\rm CB\text{-}A}(\boldsymbol{q})$. For the video illustrating the NEB determination of both LAP and MEP, see the SM [64].

in Table I. The MEP and the LAPs computed by using the NEB, EL, DPM, and DA methods are very similar. However, the DA trajectory slightly deviates from the other ones. This is because DA is more constrained by the grid spacing than DPM: regardless of the grid spacing, DA can only consider its immediate neighbors, while DPM does not have this constraint (see Fig. 3 and Sec. III B).

As indicated by Fig. 4, the final action values for the LAP obtained by the NEB, DPM, and EL methods agree well with the MEP. However, the MEP and LAP are not necessarily equivalent in general; the MEP can be viewed as an approximation of the LAP. A detailed discussion on the conditions for the MEP to be a LAP is contained in the SM [64]. To see the MEP limitations, we consider an asymmetric variant of the camel-back potential (CB-A)

$$V_{\rm CB-A}(\boldsymbol{q}) = V_{\rm CB\text{-}S}(\boldsymbol{q}) + \tfrac{1}{2}y, \tag{17}$$

where the endpoints of the local minima are $\boldsymbol{q}_{\rm in} = (1.70, -0.8)$ and $\boldsymbol{q}_{\rm fin} = (-1.70, 0.76)$. Figure 5 shows the MEP trajectory which is markedly different from the LAP solutions and corresponds to an appreciably larger action integral. Still, the MEP can be used for finding critical points (minima and saddles) on the surface.

The Müller-Brown potential is a canonical example of a PES used in theoretical chemistry [66,74,75]. The Müller-Brown surface shown in Fig. 6 is defined as

$$V_{\rm MB}(\boldsymbol{q}) = \sum_{i=1}^{4} A_i e^{a_i(x-x_{0_i})^2 + b_i(x-x_{0_i})(y-y_{0_i}) + c_i(y-y_{0_i})^2}, \tag{18}$$

where we use the same set of parameters as in Ref. [74], namely: $\boldsymbol{A} = (-200, -100, -170, 15)$, $\boldsymbol{a} = (-1, -1, -6.5, 0.7)$, $\boldsymbol{b} = (0, 0, 11, 0.6)$, $\boldsymbol{c} = (-10, -10, -6.5, 0.7)$, $\boldsymbol{x}_0 = (1, 0, -0.5, -1)$, and $\boldsymbol{y}_0 = (0, 0.5, 1.5, 1)$. The MEP follows the bent trajectory that goes through the critical points: two saddle points and one local minimum. This trajectory markedly differs from the LAPs, which are in a rough agreement. The MB surface highlights a problem with the DPM. As mentioned in Sec. III, the DPM can only search a single direction of each coordinate axis of the domain. In the case of the Muller-Brown surface,
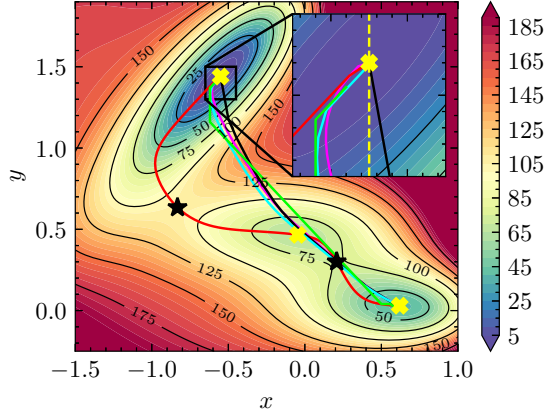
FIG. 6. Similar as in Fig. 4 but for the shifted Müller-Brown surface. The inset shows the LAP pathways close to the initial point $\boldsymbol{q}_{\text{in}}$. The yellow dashed line shows the vertical. As can be seen, all paths except for the DPM curve start by moving to the left of the vertical.
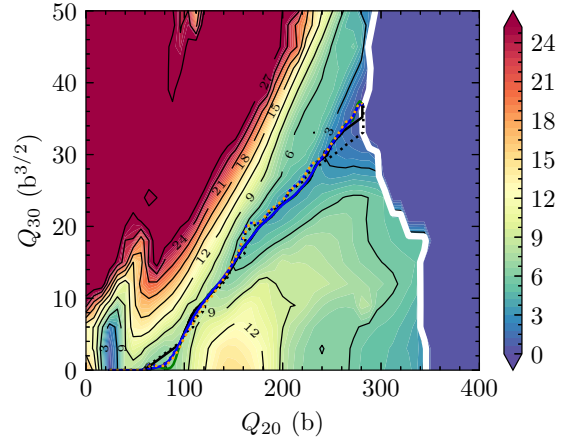

FIG. 7. The PES (in MeV) of ^{232}U in the (Q_{20}, Q_{30}) plane calculated with SkM*. Solid lines mark the LAPs and MEP obtained with the constant inertia tensor; dotted lines correspond to the nonperturbative inertia tensor. The OTL is shown in white. The blue, orange, purple, and black curves represent the LAPs calculated using the NEB, DPM, EL, and DA methods, respectively. The green curve is the MEP, which was also calculated using NEB.

the DPM cannot search for trajectories bending back in the negative-x direction. As seen in the inset of Fig. 4, the NEB, EL, and DA methods start their trajectories moving backwards in x from the initial point $\boldsymbol{q}_{\text{in}}$. The DPM path, on the other hand, always moves in the positive-x direction. Consequently, the action integral along the DPM path is slightly larger than in the other methods.

B. Realistic calculations

To illustrate the performance of the NEB method and other approaches to the LAP in realistic cases, we carried out nuclear EDF calculations for ^{232}U in two collective coordinates and ^{240}Pu in three collective coordinates. In the particle-hole channel we used the Skyrme functional SkM* [76], which is often employed in fission studies. The particle-particle interaction was approximated by the mixed density-dependent pairing force [77].

In the case of ^{232}U, we considered two collective coordinates $\boldsymbol{q} \equiv (Q_{20}, Q_{30})$ and for ^{240}Pu we took three collective coordinates $\boldsymbol{q} \equiv (Q_{20}, Q_{30}, \lambda_2)$. The axial quadrupole and octupole moment operators are defined as in Ref. [78]:

$$\hat{Q}_{\lambda 0}(r, \theta) = \mathcal{N}_\lambda \sqrt{\frac{2\lambda + 1}{4\pi}} r^\lambda P_\lambda(\cos\theta), \qquad (19)$$

where P_λ is the Legendre polynomial, $\mathcal{N}_2 = \sqrt{\frac{16\pi}{5}}$, and $\mathcal{N}_3 = 1$. The collective coordinate $\lambda_2 = \lambda_{2n} + \lambda_{2p}$ defined in Sec. II represents the dynamic pairing fluctuations. The value of $\lambda_{2\tau} = 0$ corresponds to static HFB pairing.

As in Ref. [18], to render collective coordinates dimensionless, we use dimensionless coordinates x_i defined as

$$x_i = \frac{q_i}{\delta q_i}, \qquad (20)$$

where δq_i are the scale parameters used in determining numerical derivatives of density matrices in Eq. (2). Here we took $\delta Q_{20} = 1\,\text{b}$, $\delta Q_{30} = 1\,\text{b}^{3/2}$, and $\delta \lambda_2 = 0.01\,\text{MeV}$.

1. Two-dimensional case: SF of ^{232}U

The PES was computed by solving the HFB equations using the parallel axial solver HFBTHO(v3.00) [79]. The large stretched harmonic-oscillator basis of $N = 25$ major shells was used to guarantee good convergence. We adopted a 458×501 grid with $0 \leqslant Q_{20} \leqslant 457\,\text{b}$ and $0 \leqslant Q_{30} \leqslant 50\,\text{b}^{3/2}$. To apply the NEB method, which involves local gradient calculations at arbitrary values $\boldsymbol{q}$, we interpolate the PES and the inertia tensor on the mesh. Because the grid is two-dimensional, a cubic spline interpolator suffices. Close to the $Q_{30} = 0$ axis, we take into account the mirror symmetry of the PES by setting $V(-Q_{30}) = V(Q_{30})$. Finally, since NEB updates occasionally push an image outside of the computed PES mesh, we extended the PES to grow exponentially with the distance outside the mesh, to smoothly push images back into the evaluated region.

Figure 7 shows the two-dimensional PES of ^{232}U. The least action fission pathway which goes from the g.s. at $\boldsymbol{q}_{\text{in}} = (24\,\text{b}, 0)$ to the exit point $\boldsymbol{q}_{\text{fin}} = (281\,\text{b}, 37\,\text{b}^{3/2})$ is calculated using the methods explained in Sec. III. To select the endpoint $\boldsymbol{q}_{\text{fin}}$, we compute the LAP using DPM for all points on the OTL, and select the point with the lowest action integral. This point is then used as the exit point for the other methods. While NEB does not require a fixed endpoint in general, we fix the endpoint here in order to facilitate intermethod comparison. The MEP path is calculated using the NEB method.

The action integral computed with different methods is shown in Table II. When computing the action, we interpolate the paths using a linear spline interpolator, and the action integral is computed using 500 evaluations along the path. This reduces the differences in the action that may arise from using a different number of points along the path (for instance, NEB gives a similar path to DPM using as few as 30 images). For all paths, we compute the action using the inertia tensor evaluated along the path. As can be seen, the action values computed

TABLE II. Action integrals for ^{232}U computed with different methods. The paths computed using the constant and nonperturbative inertia tensor are labeled "con." and "n.-p.," respectively.

		NEB-MEP	NEB-LAP	DPM	EL	DA
^{232}U	con.	174.5	174.2	174.2	174.9	175.8
	n.-p.		173.6	173.3	175.0	178.5
^{240}Pu	con.	19.09	18.98	19.21	19.01	22.85
	n.-p.		16.54	16.47	18.18	30.50

for ^{232}U using different methods agree well, with DA being the worst performer. As seen in Fig. 7 and Table II the MEP is very close to the LAP. This is because the static fission pathway (i.e., MEP) is fairly straight and the fission valley is well delineated. Note that perfect agreement is not expected, and in fact was not observed for the analytic surfaces, either. This is due in part to the different approximations used in each method—for DPM and DA, this is the grid spacing; for NEB, this is the number of images and approximate treatment of derivatives; and for EL, this is a variety of simplifications described in Sec. 3 in the SM [64]. Additional variation in the quality of the interpolator further hampers agreement beyond what is listed.

2. Three-dimensional case: SF of ^{240}Pu

The SF of ^{240}Pu in several collective coordinates was studied in Ref. [18] where the details pertaining to the computation, grid size, etc., can be found. Between the g.s. minimum and the fission isomer (FI), the fission pathway is affected by triaxial degrees of freedom. Between the FI and the outer turning surface (OTS), however, the predicted fission trajectory is axial. In this paper, we consider the fission of the FI of ^{240}Pu so the OTS corresponds to the FI energy.

For three-dimensional tunneling, the system of equations that must be solved to construct a global spline interpolator is too large for practical applications. Instead, we use piecewise linear interpolation. The PES at $\lambda_2 = 0$ for ^{240}Pu shown in Fig. 8 varies very smoothly in the barrier region where the potential energy is larger than the energy of the FI, and so this interpolation scheme is reasonable.

Figure 9 shows the LAPs for ^{240}Pu computed with the NEB, DPM, and EL methods in three dimensions (3D). The pathways begin at the FI minimum at $q_{\mathrm{in}} = (Q_{20}^0 = 87$ b, $Q_{30}^0 = 0$ b$^{3/2}$, $\lambda_2 = 0.0)$ and the exit point was chosen for DP in the same way as the ^{232}U results before. The NEB endpoint in this case was allowed to vary according to Eq. (13), better representing standard procedure for production runs. The exit points q_{fin} predicted by NEB (185.1 b, 18.4 b$^{3/2}$, 3.3 MeV), DPM (184.0 b, 18.6 b$^{3/2}$, 4.8 MeV) and EL (179.8 b, 17.7 b$^{3/2}$, 0.0) then differ. When the collective mass is held constant, all methods find very similar paths in the $\lambda_2 = 0.0$ plane, which are also shown in Fig. 8. The paths vary more when the nonperturbative inertia tensor is used, with the main difference between the NEB and DPM paths appearing in the region close to the FI minimum;
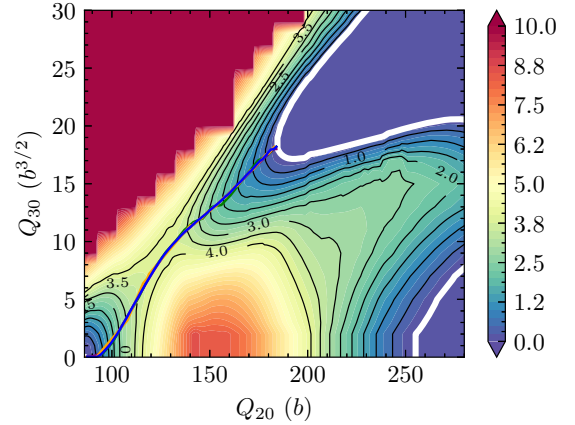

FIG. 8. The PES (in MeV) for ^{240}Pu in the space of collective coordinates Q_{20}, Q_{30} with $\lambda_2 = 0$. Only the region beyond the fission isomer is shown. The energy is normalized to the energy of the fission isomer. The OTL is shown in white. The MEP (green) practically coincides with the LAPs calculated with the constant inertia using the NEB (blue), DPM (orange), and EL (purple) methods.

beyond the saddle point, both paths are similar. As seen in Table II, the NEB and DPM are in a good agreement. In general, one would expect a better performance from NEB as this method is not constrained to a grid (this is true in the case of the analytic surfaces discussed in Sec. IV A). However, in rare cases, the DPM produces a slightly lower action than the NEB. In such cases the NEB converges to an even lower action if is initialized with the DPM result. This suggests that for tunneling in more than two dimensions (2D), a combination of NEB and DPM might be beneficial.

V. CONCLUSIONS

Finding the path that minimizes the action integral can be extremely challenging since it involves searching over the
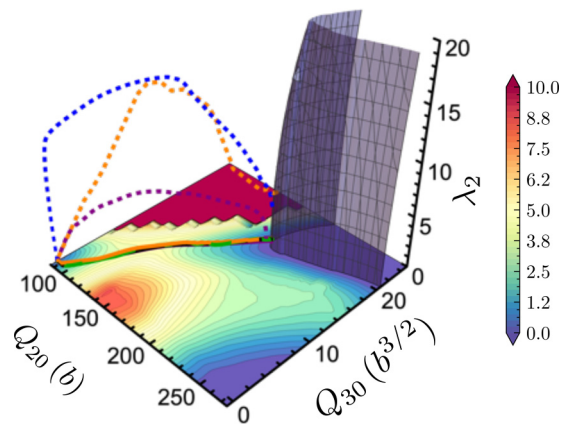

FIG. 9. The PES (in MeV) for ^{240}Pu in the collective coordinates Q_{20}, Q_{30} and λ_2. The 2D cross section at $\lambda_2 = 0$ shown in Fig. 8 is indicated. The blue, orange, and purple curves are the LAP, calculated using the NEB, DPM, and EL methods, respectively. The nonperturbative inertia tensor was used for the dashed curves. The OTS is indicated by the dark blue contour surface.

space of all continuous paths that fulfill the boundary conditions. Each method explored in this paper simplifies such task in different ways. DPM and DA project the PES onto a finite grid and explore decisions in making the path between the boundary conditions. In the EL approach the surface is modified in several ways to smooth the relation between initial conditions and the endpoint of the trajectory. The NEB method reduces the original search over continuous path into considering only piecewise linear paths, the number of pieces given by the number of images. It is this simplification that makes the NEB robust and accurate, since the total action now becomes a smooth function of the position of the images, a function that can straightforwardly be numerically minimized by gradient descent methods.

A significant advantage of the NEB is that it can accommodate any initial positions of the images, which speeds the convergence appreciably if a good prior guess of the LAP is provided. Other methods lack for such incorporation of prior knowledge. Finally, the resolution of the NEB for a rapidly varying surface can be adjusted locally by increasing the amount of images or spring constants, while for DPM and DA the entire grid resolution would have to be increased, giving an appreciable toll on the computational cost.

For both analytic and realistic potential-energy surfaces the NEB robustly produces a LAP. In the cases studied, NEB outperforms the EL and DA methods, and produces close results to those of the DPM with usually lower action integral. For many-dimensional tunneling, initiating the NEB method from the DPM path might be a winning strategy.

A huge advantage of the NEB over other methods is that it can efficiently and accurately estimate exit points. By exploring different initial conditions for the positions of the images which lead to distinct exit points, one can use the NEB method to study the phenomenon of multimodal fission. An example of such an application is shown in video 1 in the SM [64]. While other methods can find a least-action trajectory for an arbitrary final point placed on the OTL, as done, e.g., in Refs. [17–23], they cannot guarantee that this trajectory is stationary. All such trajectories can be gradually transformed into a stationary pathway by moving the final point along the OTL towards the exit point, see Fig. 2.

In this paper we also explored the minimum-energy (or static) path. We adjusted our NEB algorithm to generate MEPs, including the determination of local minima and saddle points. The necessary conditions for a MEP to also be a LAP are discussed in the SM [64]. Video 2 in the SM [64] illustrates the way the NEB method generates LAP and MEP.

An important contribution of this work is providing a beta release of the PyNEB package, a python suite of codes that implement the NEB algorithm described in this paper. The package can be found in Ref. [65] together with the respective documentation and code samples serving as a tutorial for its use. A comprehensive investigation into the intricacies of the numerical implementations and performance of the package itself will accompany the version 1.0 release.

The NEB approach can be readily paired with accelerated DFT calculations, such as the recent applications of Gaussian process regression to PES emulation [75,80]. In these works, a Gaussian process is used to emulate the PES and DFT calculations are only run if the Gaussian process is uncertain as to the actual PES value. As NEB is not a grid-based method, it can sensibly be paired with a Gaussian process emulator that is updated as necessary while NEB runs. In this way, the LAP can be determined using far fewer DFT evaluations than is necessary in DPM.

The ability to determine the exit points is essential for determining fission-fragment yields [54,55]. The minimum action provides information on SF half-lives. In this context, the NEB method described in this paper is expected to speed up the global calculations of nuclear fission for r-process simulations and studies of superheavy nuclei stability.

[1] H. J. Krappe and K. Pomorski, *Theory of Nuclear Fission*, Lecture Notes in Physics 838 (Springer Verlag, Heidelberg, 2012).

[2] K. H. Schmidt and B. Jurado, Review on the progress in nuclear fission: Experimental methods and theoretical descriptions, Rep. Prog. Phys. **81**, 106301 (2018).

[3] S. A. Giuliani, Z. Matheson, W. Nazarewicz, E. Olsen, P.-G. Reinhard, J. Sadhukhan, B. Schuetrumpf, N. Schunck, and P. Schwerdtfeger, Colloquium: Superheavy elements: Oganesson and beyond, Rev. Mod. Phys. **91**, 011001 (2019).

[4] P. Vogel, L. Wen, and C. Zhang, Neutrino oscillation studies with reactors, Nat. Commun. **6**, 6935 (2015).

[5] C. J. Horowitz, A. Arcones, B. Côté, I. Dillmann, W. Nazarewicz, I. U. Roederer, H. Schatz, A. Aprahamian, D. Atanasov, A. Bauswein, T. C. Beers, J. Bliss, M. Brodeur, J. A. Clark, A. Frebel, F. Foucart, C. J. Hansen, O. Just, A. Kankainen, G. C. McLaughlin *et al.*, r-process nucleosynthesis: Connecting rare-isotope beam facilities with the cosmos, J. Phys. G **46**, 083001 (2019).

[6] N. Vassh, R. Vogt, R. Surman, J. Randrup, T. M. Sprouse, M. R. Mumpower, P. Jaffke, D. Shaw, E. M. Holmbeck, Y.-L. Zhu, and G. C. McLaughlin, Using excitation-energy dependent fission yields to identify key fissioning nuclei in r-process nucleosynthesis, J. Phys. G **46**, 065202 (2019).

[7] S. A. Giuliani, G. Martínez-Pinedo, M.-R. Wu, and L. M. Robledo, Fission and the r-process nucleosynthesis of translead nuclei in neutron star mergers, Phys. Rev. C **102**, 045804 (2020).

[8] N. Schunck and L. M. Robledo, Microscopic theory of nuclear fission: A review, Rep. Prog. Phys. **79**, 116301 (2016).

[9] M. Bender, R. Bernard, G. Bertsch, S. Chiba, J. Dobaczewski, N. Dubray, S. A. Giuliani, K. Hagino, D. Lacroix, Z. Li, P. Magierski, J. Maruhn, W. Nazarewicz, J. Pei, S. Péru, N. Pillet, J. Randrup, D. Regnier, P.-G. Reinhard, L. M. Robledo *et al.*, Future of nuclear fission theory, J. Phys. G **47**, 113002 (2020).

[10] M. Bender, P.-H. Heenen, and P.-G. Reinhard, Self-consistent mean-field models for nuclear structure, Rev. Mod. Phys. **75**, 121 (2003).

[11] N. Schunck, *Energy Density Functional Methods for Atomic Nuclei*, IOP Expanding Physics (IOP Publishing, Bristol,2019).

[12] P. L. Kapur and R. Peierls, Penetration into potential barriers in several dimensions, Proc. R. Soc. A **163**, 606 (1937).

[13] M. Brack, J. Damgaard, A. S. Jensen, H. C. Pauli, V. M. Strutinsky, and C. Y. Wong, Funny hills: The shell-correction approach to nuclear shell effects and its applications to the fission process, Rev. Mod. Phys. **44**, 320 (1972).

[14] T. Ledergerber and H.-C. Pauli, On the dynamics of fission: The role of reflection asymmetry in the nuclear shape, Nucl. Phys. A **207**, 1 (1973).

[15] A. Baran, K. Pomorski, A. Lukasiak, and A. Sobiczewski, A dynamic analysis of spontaneous-fission half-lives, Nucl. Phys. A **361**, 83 (1981).

[16] A. Baran, Some dynamical aspects of the fission process, Phys. Lett. B **76**, 8 (1978).

[17] J. Sadhukhan, K. Mazurek, A. Baran, J. Dobaczewski, W. Nazarewicz, and J. A. Sheikh, Spontaneous fission lifetimes from the minimization of self-consistent collective action, Phys. Rev. C **88**, 064314 (2013).

[18] J. Sadhukhan, J. Dobaczewski, W. Nazarewicz, J. A. Sheikh, and A. Baran, Pairing-induced speedup of nuclear spontaneous fission, Phys. Rev. C **90**, 061304(R) (2014).

[19] J. Sadhukhan, W. Nazarewicz, and N. Schunck, Microscopic modeling of mass and charge distributions in the spontaneous fission of ^{240}Pu, Phys. Rev. C **93**, 011304(R) (2016).

[20] J. Sadhukhan, C. Zhang, W. Nazarewicz, and N. Schunck, Formation and distribution of fragments in the spontaneous fission of ^{240}Pu, Phys. Rev. C **96**, 061301(R) (2017).

[21] J. Zhao, B.-N. Lu, T. Nikć, and D. Vretenar, Multidimensionally constrained relativistic Hartree-Bogoliubov study of spontaneous nuclear fission, Phys. Rev. C **92**, 064315 (2015).

[22] J. Zhao, B.-N. Lu, T. Nikć, D. Vretenar, and S.-G. Zhou, Multidimensionally-constrained relativistic mean-field study of spontaneous fission: Coupling between shape and pairing degrees of freedom, Phys. Rev. C **93**, 044315 (2016).

[23] F. Mercier, J. Zhao, J.-P. Ebran, E. Khan, T. Nikć, and D. Vretenar, Microscopic Description of 2α Decay in ^{212}Po and ^{224}Ra Isotopes, Phys. Rev. Lett. **127**, 012501 (2021).

[24] A. Schmid, Quasiclassical wave function in multidimensional quantum decay problems, Ann. Phys. (NY) **170**, 333 (1986).

[25] U. Eckern and A. Schmid, The decay of a metastable state in a multidimensional configuration space, in *Quantum Tunnelling in Condensed Media*, Modern Problems in Condensed Matter Sciences, edited by Y. Kagan and A. Leggett (Elsevier, Amsterdam, 1992), Vol. 34, Chap. 3, pp. 145–229.

[26] T. Kindo and A. Iwamoto, Methods for the calculation of the fission half-life in the multi-dimensional space, Phys. Lett. B **225**, 203 (1989).

[27] A. Iwamoto and Y. Tomita, Adiabatic approximation in multi-dimensional penetration problem, Prog. Theor. Phys. **87**, 1171 (1992).

[28] A. Iwamoto, Multi-dimensional tunneling and nuclear fission process, Z. Phys. A: Hadrons Nucl. **349**, 265 (1994).

[29] G. Scamps and K. Hagino, Multidimensional fission model with a complex absorbing potential, Phys. Rev. C **91**, 044606 (2015).

[30] J. Skalski, Nuclear fission with mean-field instantons, Phys. Rev. C **77**, 064610 (2008).

[31] S. Levit, Variational approach to tunneling dynamics. application to hot superfluid Fermi systems. spontaneous and induced fission, Phys. Lett. B **813**, 136042 (2021).

[32] W. Brodziński and J. Skalski, Instanton-motivated study of spontaneous fission of odd-*a* nuclei, Phys. Rev. C **102**, 054603 (2020).

[33] M. Baranger, M. Strayer, and J.-S. Wu, Nuclear collective motion with full nonlinearity, Phys. Rev. C **67**, 014318 (2003).

[34] B. C. Garrett and D. G. Truhlar, A least-action variational method for calculating multidimensional tunneling probabilities for chemical reactions, J. Chem. Phys. **79**, 4931 (1983).

[35] G. Mills and H. Jónsson, Quantum and Thermal Effects in H_2 Dissociative Adsorption: Evaluation of Free Energy Barriers in Multidimensional Quantum Systems, Phys. Rev. Lett. **72**, 1124 (1994).

[36] G. Mills, H. Jónsson, and G. K. Schenter, Reversible work transition state theory: Application to dissociative adsorption of hydrogen, Surf. Sci. **324**, 305 (1995).

[37] H. Jónsson, G. Mills, and K. W. Jacobsen, Nudged elastic band method for finding minimum energy paths of transitions, in *Classical and Quantum Dynamics in Condensed Phase Simulations*, edited by B. J. Berne, G. Ciccotti, and D. F. Coker (World Scientific, 1998), pp. 385–404.

[38] G. Henkelman, B. P. Uberuaga, and H. Jónsson, A climbing image nudged elastic band method for finding saddle points and minimum energy paths, J. Chem. Phys. **113**, 9901 (2000).

[39] G. Henkelman and H. Jónsson, Improved tangent estimate in the nudged elastic band method for finding minimum energy paths and saddle points, J. Chem. Phys. **113**, 9978 (2000).

[40] The Atomic Simulation Environment Documentation, https://wiki.fysik.dtu.dk/ase/ase/neb.html.

[41] B. Peters, A. Heyden, A. T. Bell, and A. Chakraborty, A growing string method for determining transition states: Comparison to the nudged elastic band and string methods, J. Chem. Phys. **120**, 7877 (2004).

[42] A. Mamdouh, J. Pearson, M. Rayet, and F. Tondeur, Large-scale fission-barrier calculations with the ETFSI method, Nucl. Phys. A **644**, 389 (1998).

[43] P. Möller, D. G. Madland, A. J. Sierk, and A. Iwamoto, Nuclear fission modes and fragment mass asymmetries in a five-dimensional deformation space, Nature (London) **409**, 785 (2001).

[44] A. Iwamoto, P. Möller, D. G. Madland, and A. J. Sierk, Mass division in nuclear fission and isotope effect, J. Nucl. Sci. Technol. (Abingdon, U. K.) **39**, 332 (2002).

[45] P. Möller, A. J. Sierk, and A. Iwamoto, Five-Dimensional Fission-Barrier Calculations from ^{70}Se to ^{252}Cf, Phys. Rev. Lett. **92**, 072501 (2004).

[46] Z.-M. Wang, W.-J. Zhu, X. Zhu, C.-L. Zhong, and T.-S. Fan, ^{236}U multi-modal fission paths on a five-dimensional deformation surface, Commun. Theor. Phys. **71**, 417 (2019).

[47] V. Ásgeirsson, B. O. Birgisson, R. Bjornsson, U. Becker, F. Neese, C. Riplinger, and H. Jónsson, Nudged elastic band method for molecular reactions using energy-weighted springs combined with eigenvector following, J. Chem. Theory Comput. **17**, 4929 (2021).

[48] D. Sheppard, R. Terrell, and G. Henkelman, Optimization methods for finding minimum energy paths, J. Chem. Phys. **128**, 134106 (2008).

[49] J. J. Moré and T. S. Munson, Computing mountain passes and transition states, Math. Program. **100**, 151 (2004).

[50] N. L. Vaquero, T. R. Rodríguez, and J. L. Egido, On the impact of large amplitude pairing fluctuations on nuclear spectra, Phys. Lett. B **704**, 520 (2011).

[51] N. L. Vaquero, J. L. Egido, and T. R. Rodríguez, Large-amplitude pairing fluctuations in atomic nuclei, Phys. Rev. C **88**, 064311 (2013).

[52] M. Warda, A. Staszczak, and W. Nazarewicz, Fission modes of mercury isotopes, Phys. Rev. C **86**, 024601 (2012).

[53] J. Berger, M. Girod, and D. Gogny, Microscopic analysis of collective dynamics in low energy fission, Nucl. Phys. A **428**, 23 (1984).

[54] J. Sadhukhan, S. A. Giuliani, Z. Matheson, and W. Nazarewicz, Efficient method for estimation of fission fragment yields of *r*-process nuclei, Phys. Rev. C **101**, 065803 (2020).

[55] J. Sadhukhan, S. A. Giuliani, and W. Nazarewicz, Theoretical description of fission yields: Toward a fast and efficient global model, Phys. Rev. C **105**, 014619 (2022).

[56] A. Baran, J. A. Sheikh, J. Dobaczewski, W. Nazarewicz, and A. Staszczak, Quadrupole collective inertia in nuclear fission: cranking approximation, Phys. Rev. C **84**, 054321 (2011).

[57] S. A. Giuliani and L. M. Robledo, Non-perturbative collective inertias for fission: A comparative study, Phys. Lett. B **787**, 134 (2018).

[58] K. Washiyama, N. Hinohara, and T. Nakatsukasa, Finite-amplitude method for collective inertia in spontaneous fission, Phys. Rev. C **103**, 014306 (2021).

[59] A. Baran, Z. Łojewski, K. Sieja, and M. Kowal, Global properties of even-even superheavy nuclei in macroscopic-microscopic models, Phys. Rev. C **72**, 044310 (2005).

[60] W. Quapp and D. Heidrich, Analysis of the concept of minimum energy path on the potential energy surface of chemically reacting systems, Theor. Chim. Acta **66**, 245 (1984).

[61] N. Dubray and D. Regnier, Numerical search of discontinuities in self-consistent potential energy surfaces, Comput. Phys. Commun. **183**, 2035 (2012).

[62] A. Zdeb, M. Warda, and L. M. Robledo, Description of the multidimensional potential-energy surface in fission of ^{252}Cf and ^{258}No, Phys. Rev. C **104**, 014610 (2021).

[63] N.-W. T. Lau, R. N. Bernard, and C. Simenel, Smoothing of 1D and 2D discontinuities in potential energy surfaces, Phys. Rev. C **105**, 034617 (2022).

[64] See Supplemental Material at http://link.aps.org/supplemental/10.1103/PhysRevC.105.054302 for the algorithms, videos, and details on MEP and LAP equivalence conditions, and the Euler-Lagrange implementation.

[65] See https://pyneb.dev.

[66] V. Ásgeirsson, A. Arnaldsson, and H. Jónsson, Efficient evaluation of atom tunneling combined with electronic structure calculations, J. Chem. Phys. **148**, 102334 (2018).

[67] L. Verlet, Computer "experiments" on classical fluids. I. Thermodynamical properties of Lennard-Jones molecules, Phys. Rev. **159**, 98 (1967).

[68] E. Bitzek, P. Koskinen, F. Gähler, M. Moseler, and P. Gumbsch, Structural Relaxation Made Simple, Phys. Rev. Lett. **97**, 170201 (2006).

[69] J. Guénolé, W. G. Nöhring, A. Vaid, F. Houllé, Z. Xie, A. Prakash, and E. Bitzek, Assessment and optimization of the fast inertial relaxation engine (FIRE) for energy minimization in atomistic simulations and its implementation in LAMMPS, Comput. Mater. Sci. **175**, 109584 (2020).

[70] E. W. Dijkstra, A note on two problems in connexion with graphs, Numer. Math. **1**, 269 (1959).

[71] R. Weinstock, *Calculus of Variations: With Applications to Physics and Engineering* (Dover Publications, Inc., New York, 1974).

[72] Numerical Solution of Boundary Value Problems (BVP), https://reference.wolfram.com/language/tutorial/NDSolveBVP.html.

[73] V. Lakshminarayanan and S. Varadharajan, Dynamic programming, the Fermat principle, and the eikonal equation revisited, J. Optim. Theory Appl. **95**, 713 (1997).

[74] K. Müller and L. D. Brown, Location of saddle points and minimum energy paths by a constrained simplex optimization procedure, Theor. Chim. Acta **53**, 75 (1979).

[75] O.-P. Koistinen, F. B. Dagbjartsdóttir, V. Ásgeirsson, A. Vehtari, and H. Jónsson, Nudged elastic band calculations accelerated with Gaussian process regression, J. Chem. Phys. **147**, 152720 (2017).

[76] J. Bartel, P. Quentin, M. Brack, C. Guet, and H.-B. Håkansson, Towards a better parametrisation of Skyrme-like effective forces: A critical study of the SkM force, Nucl. Phys. A **386**, 79 (1982).

[77] J. Dobaczewski, W. Nazarewicz, and M. V. Stoitsov, Nuclear ground-state properties from mean-field calculations, Eur. Phys. J. A **15**, 21 (2002).

[78] J. Dobaczewski and P. Olbratowski, Solution of the Skyrme–Hartree–Fock–Bogolyubov equations in the cartesian deformed harmonic-oscillator basis. (IV) HFODD (v2.08i): A new version of the program, Comput. Phys. Commun. **158**, 158 (2004).

[79] R. Navarro Perez, N. Schunck, R.-D. Lasseri, C. Zhang, and J. Sarich, Axially deformed solution of the Skyrme–Hartree–Fock–Bogolyubov equations using the transformed harmonic oscillator basis (III) HFBTHO (v3.00): A new version of the program, Comput. Phys. Commun. **220**, 363 (2017).

[80] J. A. Garrido Torres, P. C. Jennings, M. H. Hansen, J. R. Boes, and T. Bligaard, Low-Scaling Algorithm for Nudged Elastic Band Calculations Using a Surrogate Machine Learning Model, Phys. Rev. Lett. **122**, 156001 (2019).